

Analysis of the flow in gravity currents propagating up a slope

L. Ottolenghi^{a,*}, C. Adduce^a, F. Roman^b, V. Armenio^c

^a*Department of Engineering, University Roma Tre, Rome, 00146, Italy*

^b*Iefluids, Piazzale Europa 1, 34127, Trieste, Italy*

^c*Department of Engineering and Architecture, University of Trieste, Trieste, 34127, Italy*

Abstract

Lock-release gravity currents flowing up a slope are investigated by Large Eddy Simulations. The angle between the bottom boundary and the horizontal direction, θ , and the aspect ratio of the initial volume of dense fluid in the lock, R , are varied. The mean flow is analysed and both density and velocity fields reveal the presence of a backward flow close to the bottom of the domain directed to the lock region. The intensity of the backward flow is discussed in terms of both streamwise velocity component and negative flow discharge. The analysis of the friction velocity at the bottom is also presented, showing the role of the tail region of gravity currents propagating up a slope in sediment transport. Turbulent structures developing in the near-wall region and the budget of the turbulent kinetic energy are analysed in order to investigate the regions of the gravity current in which turbulence is more pronounced. The analysis shows that at the beginning of the process, turbulent quantities have a stronger intensity especially in the areas where Kelvin-Helmholtz billows develop. When these structures lose their coherence, three-dimensional features of the flow appear more evident and the turbulence intensity decreases, still remaining well active in the head of the gravity current, at the interface between the two fluids.

Keywords: Buoyancy-driven flows, Large Eddy Simulation, Gravity current

*Corresponding author

Email addresses: luisa.ottolenghi@uniroma3.it (L. Ottolenghi),
claudia.adduce@uniroma3.it (C. Adduce)

1 **1. Introduction**

2 Gravity currents develop when a dense fluid flows into an ambient fluid of
3 lower density mainly in the horizontal direction. The buoyancy gradient between
4 the two fluids drives the motion and can be due to differences in the temperature
5 or in the concentration fields. When the density difference is provided by the
6 presence of suspended solid particles into the body of the current, the flow is
7 more properly referred to as turbidity current. These phenomena widely occur
8 in the environment (oceanic overflows, sea breeze fronts, avalanches, submarine
9 landslides) and examples of these flows with their environmental implications
10 are presented in Simpson (1997).

11 Steady and unsteady gravity currents develop when a constant discharge or a
12 fixed volume of dense fluid are released into a lighter ambient fluid. In the en-
13 vironment, unsteady underflows can be generated by seismogenic slumping and
14 pyroclastic flows following an earthquake. The mobilization of ancient deposits
15 and sediments causes the generation of turbidity currents whose behaviour and
16 dynamics are important for the formation of new sedimentation reservoir (as
17 hydrocarbon reservoirs), for submarine cable breakages, and for the potential
18 environmental hazards they pose (Kneller et al., 1999). The release of pollu-
19 tants in the sea and the dispersion of fluvial discharges (Inghilesi et al., 2012)
20 are other examples of gravity currents whose location, velocity of propagation
21 and density concentration are essential information for the environmental pro-
22 tection (Kneller & Buckee, 2000).

23 Unsteady gravity currents can be numerically reproduced through the lock-
24 exchange technique, which is applied filling a domain, divided into two different
25 volumes, with two fluids of different densities. At the beginning of the sim-
26 ulation, the two fluids interact with each other, the heavier fluid starts flow-
27 ing on the bottom of the domain and the ambient fluid flows backward by

28 continuity. During the development of the current, different flow regimes are
29 observed (Rottman & Simpson, 1983): a slumping phase, a self-similar phase,
30 and an eventual viscous phase. According to the shallow water theory, during
31 the slumping phase the dense current propagates at a constant velocity, while
32 during the following regimes the front of the current decelerates, following the
33 theoretical power laws proportional to $t^{2/3}$ (self-similar phase) and $t^{1/5}$ (viscous
34 phase).

35 Lock-exchange gravity currents are numerically simulated in order to gain de-
36 tailed information about the density and velocity fields of the flow by apply-
37 ing different kind of high-resolution numerical models solving the Boussinesq
38 form of the Navier-Stokes equations. Direct Numerical Simulations (DNS) and
39 Large Eddy Simulations (LES) were performed to study and unsteady grav-
40 ity currents in different configurations (Härtel et al., 2000; Cantero et al., 2007,
41 2008; Ooi et al., 2009; Özgökmen et al., 2009; Tokyay et al., 2011; Ilıcak, 2014;
42 Ottolenghi et al., 2016a). A thorough description of the motion, including en-
43 ergy budgets and analysis of turbulent structures was obtained by the available
44 high-resolved flow fields. In particular, these investigations focused on the study
45 of wall-shear stresses, drag and lift forces, on the effects of submerged obstacles
46 on the flow dynamics and on the evaluation of mixing at different Reynolds
47 numbers.

48 Gravity currents on horizontal and down-sloping bottoms were investigated by
49 several numerical and laboratory studies realized in order to gain information
50 about the dynamics of the current and quantify mixing with the ambient fluid
51 (Chang et al., 2005; Özgökmen et al., 2006; Legg et al., 2006; Adduce et al.,
52 2012; Dai, 2013; Dai & Huang, 2016; La Rocca et al., 2013). On the other hand,
53 only few studies were dedicated to the investigation of gravity currents flowing
54 up a slope, although this latter case frequently occurs in the environment: sea
55 breeze fronts can propagate over irregular coastal inlands, oceanic flows com-
56 monly develop along complex bathymetries and salt water intrusion occurs into
57 estuaries. Further, the passage of gravity currents on the irregular oceanic bot-
58 tom is frequently related to erosive phenomena and plays a determinant role

59 in sediment transport. Laboratory experiments of unsteady gravity currents
60 propagating first along a horizontal bottom and then up a slope were performed
61 by Marleau et al. (2014). They observed that the reduced gravity driving the
62 motion, the inclination of the slope and the ratio between the initial depth
63 of the dense and the ambient fluids affected the flow. The front velocity of
64 gravity currents propagating both horizontally and up a small slope was inves-
65 tigated by both laboratory experiments and hydrostatic numerical simulations
66 by Jones et al. (2015). Further, laboratory experiments and shallow water simu-
67 lations of up-sloping gravity currents were performed by Lombardi et al. (2015),
68 who found the deceleration of the dense current to be dependent on the ups-
69 slope only after the transition from the slumping to the self-similar regime. In
70 Safrai & Tkachenko (2009) LES were performed varying the inclination of the
71 bottom, and also two up-sloping angles were considered ($\theta = 5^\circ$, $\theta = 10^\circ$): a
72 less energetic three-dimensional turbulent pattern of the gravity current flowing
73 up the slope and the tendency of the motion to be more two-dimensional were
74 observed if compared to the down-sloping cases. Finally, in Ottolenghi et al.
75 (2016b) (hereafter OAIRA16) entrainment and mixing in dense currents prop-
76 agating up a slope were investigated by LES. Also in this latter study, the
77 dependence of the front velocity on the upslope was observed during the self-
78 similar phase, and mixing and entrainment were found to be reduced with the
79 increase of the upslope. Here, we take advantage of the database generated in
80 OAIRA16 to investigate the effect of an upslope on the near bed dynamics and
81 the implications on sediment transport. Then, the aim of the present study
82 is the investigation of both turbulent and mean flow quantities in lock-release
83 gravity currents propagating up a sloping bottom. The analysis is performed by
84 LES and particular attention is paid to the dynamics of the bottom region, in
85 order to investigate possible implications of gravity currents on sediment trans-
86 port. The three-dimensional highly-resolved density and velocity fields gained
87 by the numerical simulations allow to address several scientific questions about
88 the dynamics of an up-sloping gravity current. How does an up-sloping bed
89 affect the mean flow of a gravity current and the potential to transport sedi-

90 ments? Which are the regions in an up-sloping gravity current more involved
91 in the processes of production-dissipation of turbulence? How do the terms in-
92 volved in the turbulent kinetic energy balance evolve during the propagation of
93 the dense current?

94 The present paper is organized as follows. The problem formulation and the
95 numerical model are presented in section 2; in section 3 results are reported and
96 discussed; conclusions are given in section 4.

97 **2. Problem formulation and numerical model**

98 The lock-exchange configuration is numerically reproduced in order to inves-
99 tigate the dynamics of unsteady gravity currents flowing up a sloping bottom
100 (Fig. 1).

101 The numerical domain is characterized by a length $L = 3$ m, a height $H = 0.2$
102 m and a width $d = 0.2$ m in the x , y and z directions, respectively, where
103 x is oriented along the streamwise direction, y is the bottom-wall normal di-
104 rection and z is the spanwise one. The computational grid is composed of
105 $2048 \times 128 \times 64$ cells, in the x , y and z directions, respectively. The grid spac-
106 ings are $\Delta x = 0.01H$, $\Delta z = 0.016H$ and Δy ranges from $0.01H$ at the top,
107 to $0.002H$ at the bottom of the domain (which were verified to be sufficient to
108 resolve the viscous sublayer, avoiding the use of wall layer models).

109 A vertical discontinuity in the initial density field is located at a distance x_0
110 from the left wall of the domain in the streamwise direction, in order to divide
111 the numerical domain into two volumes. Dense fluid of density ρ_1 fills the vol-
112 ume on the left-hand side of the discontinuity (the lock region) while ambient
113 fluid of density $\rho_0 < \rho_1$ fills the rest of the domain. The simulation begins
114 allowing the interaction between the two fluids, and a gravity current develops:
115 the dense fluid propagates rightwards along the bottom of the domain, and the
116 ambient fluid above flows leftwards by continuity. The initial water depths of
117 the dense and the ambient fluids are h_0 and H , respectively, and full-depth
118 gravity currents are generated, i.e. $h_0 = H$. The initial aspect ratio of the lock

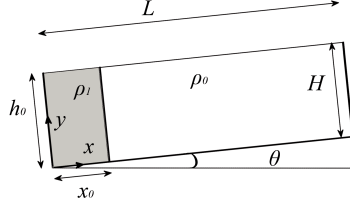


Figure 1: Sketch of the lock-exchange configuration.

119 volume $R = H/x_0$ is varied by changing x_0 ($R = 2$, $R = 1$ and $R = 0.67$). The
 120 angle between the bottom boundary and the horizontal direction, θ , is varied
 121 in order to investigate the effect of an up-sloping bottom on the flow dynamics
 122 ($\theta = 0^\circ$, $\theta = 1.4^\circ$, $\theta = 2.5^\circ$ and $\theta = 5^\circ$). The slope of the bottom is defined as
 123 $s = \tan \theta$.

124 The initial buoyancy gradient driving the motion is kept constant in all the
 125 simulations, by fixing $\rho_0 = 1000 \text{ kg/m}^3$ and $\rho_1 = 1030 \text{ kg/m}^3$. The resulting
 126 initial reduced gravity is $g'_0 = 0.29 \text{ ms}^{-2}$, which is defined as:

$$g'_0 = g \frac{\rho_1 - \rho_0}{\rho_0} \quad (1)$$

127 The Reynolds number characterizing the flow is $\text{Re}=48522$, and it is defined
 128 as:

$$\text{Re} = \frac{u_b H}{\nu} \quad (2)$$

129 where ν is the kinematic viscosity and u_b is the buoyancy velocity, defined as:

$$u_b = \sqrt{g'_0 H} \quad (3)$$

130 Eight LES are performed varying θ and R (RUN0 \div RUN7), which are
 131 summarized in Table 1.

132 The numerical model of Armenio & Sarkar (2002), widely validated and em-
 133 ployed over the years (Taylor et al., 2005; Ottolenghi et al., 2016a,b), is used
 134 in the present study. The numerical model solves the Boussinesq form of the

135 filtered Navier-Stokes equations (LES filtering operation is marked with the
136 symbol $\bar{\square}$):

$$\frac{\partial \bar{u}_j}{\partial x_j} = 0 \quad (4)$$

$$\frac{\partial \bar{u}_i}{\partial t} + \frac{\partial \bar{u}_j \bar{u}_i}{\partial x_j} = -\frac{1}{\rho_0} \frac{\partial \bar{p}}{\partial x_i} + \frac{\partial}{\partial x_j} \left(\nu \frac{\partial \bar{u}_i}{\partial x_j} \right) - \frac{\rho'}{\rho_0} g \delta_{ij=1,2} - \frac{\partial \tau_{ij}}{\partial x_j} \quad (5)$$

$$\frac{\partial \bar{s}}{\partial t} + \frac{\partial \bar{u}_j \bar{s}}{\partial x_j} = \frac{\partial}{\partial x_j} \left(k_s \frac{\partial \bar{s}}{\partial x_j} \right) - \frac{\partial \lambda_j}{\partial x_j} \quad (6)$$

137 where u_i are the velocity components along the x , y and z directions. The
138 hydrodynamic pressure is p and the salinity is denoted as s . The terms ν and
139 k_s in (5) and (6) are the kinematic viscosity and the molecular salt diffusivity,
140 respectively. ρ' is the variation of density with respect to the reference value ρ_0
141 (corresponding to the reference salinity s_0). Since the field is isothermal, the
142 state equation reads as:

$$\rho = \rho_0 [1 + \beta(s - s_0)] \quad (7)$$

143 where β is the salinity contraction coefficient. The effects of the inclined bottom
144 are numerically modelled by separating the gravitational acceleration g into
145 two components (δ_{ij}), oriented along the x -axis and the y -axis, respectively
146 (Dai et al., 2012; Dai, 2013, 2015; Ottolenghi et al., 2016b):

$$\delta_{ij} = \begin{cases} \sin \theta & \text{if } i = j = 1 \rightarrow x\text{-direction} \\ \cos \theta & \text{if } i = j = 2 \rightarrow y\text{-direction} \\ 0 & \text{if } i = j = 3 \rightarrow z\text{-direction} \\ 0 & \text{if } i \neq j \end{cases} \quad (8)$$

147 Further details about the model and the subgrid stresses implementation
148 are given in OAIRA2016, while a description of initial and boundary conditions
149 employed is here reported for completeness. Flat, no-slip surfaces are set at
150 $x = 0$, $x = L$ and $y = 0$. A shear-free boundary condition is applied at the top
151 boundary ($y = H$). Periodicity is employed in the spanwise direction. Zero flux

| NAME | θ ($^{\circ}$) | s | x_0 (m) | R |
|------|----------------------------|--------|--------------|------|
| RUN0 | 0.0 | 0.0 | 0.10 | 2 |
| RUN1 | 1.4 | 0.0244 | 0.10 | 2 |
| RUN2 | 2.5 | 0.0437 | 0.10 | 2 |
| RUN3 | 5.0 | 0.0875 | 0.10 | 2 |
| RUN4 | 1.4 | 0.0244 | 0.20 | 1 |
| RUN5 | 2.5 | 0.0437 | 0.20 | 1 |
| RUN6 | 1.4 | 0.0244 | 0.30 | 0.67 |
| RUN7 | 2.5 | 0.0437 | 0.30 | 0.67 |

Table 1: Parameters of numerical simulations.

152 of the scalar is imposed at all the boundaries.

153 The time step of the simulations is calculated assuring a constant value of the
154 Courant number equal to 0.6. The Schmidt number, defined as the ratio between
155 the kinematic viscosity and the molecular diffusivity, is equal to 600, which is
156 the reference value for salty water.

157 The flow field is initialized with the fluid at rest everywhere. A spatial dis-
158 tribution of the scalar is given at $t = 0$: $\rho = \rho_1$ for $x < x_0$ and $\rho = \rho_0$ for
159 $x \geq x_0$.

160 3. Results and discussion

161 3.1. The flow topology

162 In order to analyse the dynamics of gravity currents flowing up a sloping
163 bottom, the dimensionless density field ρ^* is defined as:

$$\rho^*(x, y, z, t) = \frac{\rho(x, y, z, t) - \rho_0}{\rho_1 - \rho_0} \quad (9)$$

164 The development of a lock-release gravity current can be considered mainly
165 two-dimensional and thus averaged quantities along the spanwise direction of
166 homogeneity ($\langle \rho^* \rangle$ and $\langle u \rangle$) are analysed to describe the mean flow. In order to

167 be consistent with previous studies (Nogueira et al., 2013b,a; Ottolenghi et al.,
168 2016a,b), the isopycnal $\langle \rho^* \rangle = 0.02$ is used as interface between the gravity
169 current and the ambient fluid.

170 During the propagation of a gravity current on a horizontal bed, the ambient
171 fluid is entrained into the body of the current, where a decrease in density occurs
172 due to dilution (Ottolenghi et al., 2016a). The decrease in density reduces the
173 magnitude of the buoyancy force and the flow slows down. In the up-sloping
174 cases the buoyancy force is eventually overcome by the component of the gravity
175 force parallel to the sloping bottom, which acts against buoyancy. The evolution
176 in time of the dimensionless density field, $\langle \rho^* \rangle$, for RUN3 ($\theta = 5^\circ$ and $R = 2$)
177 is shown in Fig. 2. Kelvin-Helmholtz billows are visible during the slumping
178 phase (Fig. 2a). In the following self-similar phase, the interface dividing the
179 dense and the ambient fluids becomes smoother and the thickness of the gravity
180 current decreases (Figs. 2b and 2c). Furthermore, while the head of the current
181 propagates downstream, part of the tail of the dense current starts to flow
182 backward, due to the upslope. Thus, high values of density are observed in the
183 left part of the domain, where an accumulation region develops (Figs. 2c and 2d)
184 (Lombardi et al., 2015; Marleau et al., 2014; Ottolenghi et al., 2016b).

185 The spanwise-averaged streamwise velocity component $\langle u \rangle$ at $T^* \cong 65$ (cor-
186 responding to a fully developed self-similar regime for the $R = 2$ cases) is shown
187 in Fig. 3 for RUN0÷RUN3. In the figure, $\langle u \rangle$ is made dimensionless with u_b . As
188 expected, the increase of the upslope slows down the dense current and makes
189 the position of the front more and more rearward. In the horizontal-bed case
190 (Fig. 3a) positive values of $\langle u \rangle$ are found in the head and in the body regions
191 of the gravity current while, by continuity, the ambient fluid flows backwards.
192 The highest values of $\langle u \rangle$ are found in the head region, decreasing in magni-
193 tude along the body of the current and reaching the lowest values in the tail
194 region. The same features are detectable in the up-sloping runs (Figs. 3b-d)
195 with smaller velocities. In Figs. 3b-d, negative values of $\langle u \rangle$ are also visible
196 in the tail region close to the bottom of the domain. The backward flow is
197 more pronounced at higher θ . In the tail region close to the interface with the

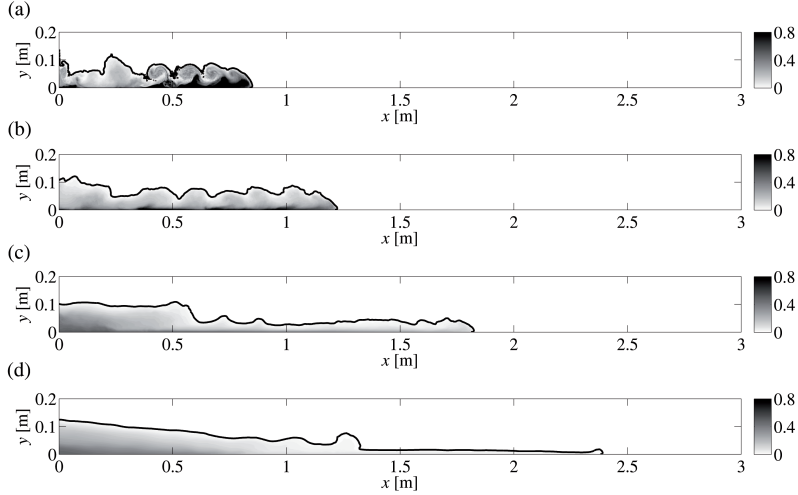


Figure 2: Dimensionless density field at different times for RUN3 ($\theta = 5^\circ$, $R = 2$): (a) $T^* = 18.6$; (b) $T^* = 31.3$; (c) $T^* = 65.4$; (d) $T^* = 145.7$.

198 ambient fluid, positive values of $\langle u \rangle$ are also visible. In fact, part of the dense
 199 fluid propagating backward reaches the left wall of the domain, rebounds, and
 200 starts moving downstream again. In RUN3, after $T^* = 65$, most of the dense
 201 fluid flows backward and stratifies at the beginning of the domain; only a thin
 202 gravity current continues to climb up the slope, becoming thinner and thinner,
 203 until it completely stops, before reaching the right wall of the domain.

204 In order to quantify the intensity of the backward flow, the positive flow, Q^+ ,
 205 the negative flow, Q^- , and the net flow, Q_n , are evaluated for each simulation
 206 as the flows crossing a bottom wall-normal section into the tail region of the
 207 gravity currents:

$$Q_n(t) = \int_{h(x,t)} \langle u(x,y,t) \rangle dh(x,t) \quad (10)$$

208 where $h(x,t)$ is the height of the current. Q^+ and Q^- are the positive and nega-
 209 tive contributions of Q_n , respectively. The streamwise location of this section is
 210 chosen by analysing the dynamic function $W(x,t)$, defined as in Nogueira et al.
 211 (2014):

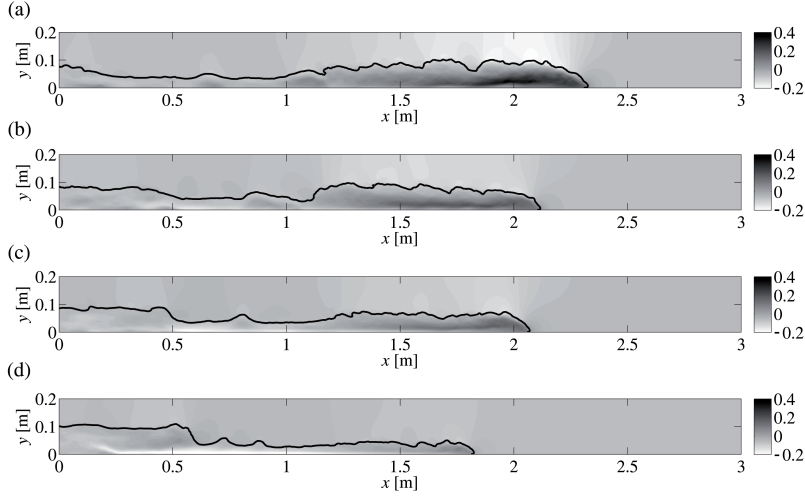


Figure 3: $\langle u \rangle$ velocity component for different numerical simulations ($R = 2$ cases) at $T^* \cong 65$: (a) RUN0 ($\theta = 0^\circ$); (b) RUN1 ($\theta = 1.4^\circ$); (c) RUN2 ($\theta = 2.5^\circ$); (d) RUN3 ($\theta = 5^\circ$). $\langle u \rangle$ is made dimensionless with u_b in all the panels.

$$W(x, t) = \langle \rho_v(x, t) \rangle \cdot h(x, t) \quad (11)$$

212 where $\langle \rho_v(x, t) \rangle$ is the depth-averaged density. The tail region of gravity cur-
 213 rents propagating on horizontal boundaries is characterized by low values of
 214 density and reduced h . For gravity currents propagating up a sloping bottom,
 215 W is high in the head and body regions, decreases in the tail region and increases
 216 again in the accumulation region. The section into the tail region chosen to eval-
 217 uate the flow rates is positioned at the first meaningful local minimum of W ,
 218 behind the body region. Fig. 4 shows the flows during the advancement of the
 219 gravity currents with $R = 2$. At the beginning of the simulations high values of
 220 Q^+ are found, due to the formation of the dense current. During the slumping
 221 phase, both positive and negative values of the flow are observed. After the
 222 transition to the self-similar phase ($(x - x_0)/H \simeq 4$ in Fig. 4) the tail region
 223 of the gravity current is well-defined and increases in length, and the backward
 224 flow is clearly detectable. During the self-similar phase, the net flow Q_n in the
 225 tail region of gravity currents flowing up a slope is negative, indicating that the

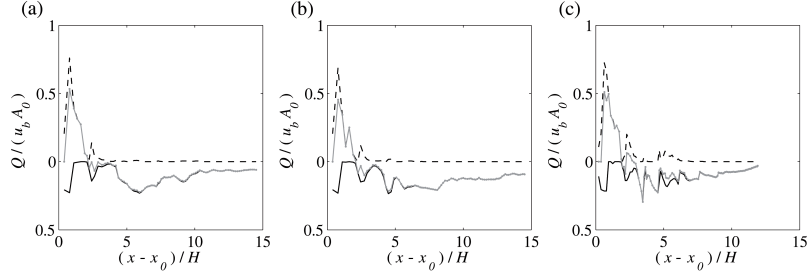


Figure 4: Q^+ (dashed lines), Q^- (solid black lines) and Q_n (grey lines) versus $(x - x_0)/H$. (a) RUN1 ($\theta = 1.4^\circ$, $R = 2$); (b) RUN2 ($\theta = 2.5^\circ$, $R = 2$); (c) RUN3 ($\theta = 5^\circ$, $R = 2$).

226 rear part of the current is not feeding the head region during its advancement
 227 but, conversely, the part of dense current propagating forward is decreasing in
 228 volume. The effect of the slope on Q^- is visible by comparing Figs. 4a, 4b and
 229 4c. The intensity of the backward flow seems to be not affected by s ; in fact,
 230 while the velocities increase with s (Fig. 3), the tail region becomes thinner
 231 and thinner and the resulting Q^- remain of the same magnitude. However, in
 232 the case with $\theta = 5^\circ$ Q^- tends to zero at the end of the simulation (Fig. 4c):
 233 the height of the dense current climbing the slope becomes very thin, until the
 234 current stops at the end of the simulation and the dense fluid spread over the
 235 slope retreats (Fig. 2d). Also when $R = 1$ and $R = 0.67$ positive values of Q_n
 236 are observed at the beginning of the simulations (not shown). The backward
 237 flow is clearly detected after $(x - x_0)/H \simeq 5$ for the $R = 1$ cases and after
 238 $(x - x_0)/H \simeq 6$ for the $R = 0.67$ cases, i.e. before the transition to the self-
 239 similar phase. This indicates that, after an initial formation and development
 240 of the dense current, once the structure of the tail region is well-defined, the
 241 backward flow is always detected and it is not affected by R .

242 3.2. The wall-shear stress

243 The friction velocity u_τ is analysed in this section in order to study the
 244 potential of gravity currents flowing up a slope to erode the bottom boundary
 245 and transport sediments. The sediments transport occurs when the shear stress
 246 at the bottom is higher than the critical shear stress for the initiation of motion,

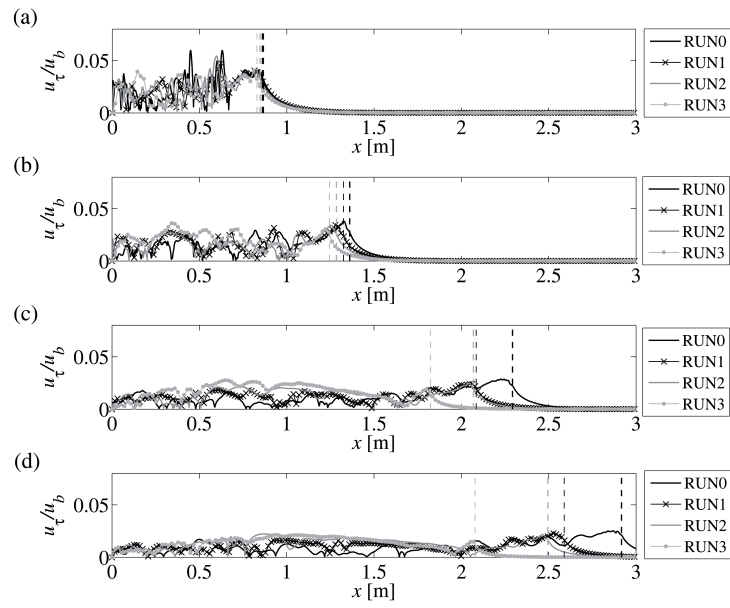


Figure 5: Dimensionless friction velocity at different times for the runs with $R = 2$: effect of the variation of θ . (a) $T^* \simeq 8$; (b) $T^* \simeq 32$; (c) $T^* \simeq 65$; (d) $T^* \simeq 90$. Vertical dashed lines mark the front position of the gravity currents.

247 which is related to the characteristic diameter and the nature of the sediments.
 248 u_τ is defined as:

$$u_\tau = \sqrt{\frac{|\tau|}{\rho}} \quad (12)$$

249 where τ is the bed shear stress ($\tau = \mu \frac{d(u)}{dy} \Big|_{y=0}$). The friction velocity made
 250 dimensionless with u_b is shown in Fig. 5 for the cases with $R = 2$. Fig. 5a shows
 251 the dimensionless u_τ during the slumping phase. The highest values of u_τ/u_b are
 252 observed in the head region of the gravity currents and in the body region when
 253 coherent and strong Kelvin-Helmholtz billows reach the bottom boundary layer.
 254 After the transition to the self-similar regime, the front positions of the gravity
 255 currents with different θ diversify (dashed vertical lines in Figs. 5b-d) and, for
 256 all cases considered, the dimensionless friction velocity in the head region of the
 257 gravity currents decreases in time. For the upsloping cases, high values of the
 258 dimensionless u_τ are visible in the tail region of the gravity currents and are
 259 related to the presence of the backward flow. These values increase in time and
 260 with increasing θ (Figs. 5b-d). In fact, in RUN3 the values of u_τ/u_b observed
 261 in the tail region are higher than those observed in the head region (Figs. 5c
 262 and 5d). This indicates that for RUN3, i.e. a gravity current flowing up a slope
 263 with $\theta = 5^\circ$, the tail of the current has a higher potential to transport sediments
 264 if compared to the head of the current. In addition, since a back flow occurs
 265 in the tail region, in this region the sediments can be transported downslope,
 266 while the current is still moving upslope.
 267 Finally, in Fig. 6 the dimensionless u_τ is shown for different runs with the same
 268 $\theta = 1.4^\circ$. As expected, u_τ/u_b increases for low values of R ; this is visible in
 269 the whole dense current, i.e both in the head, the body and the tail regions. In
 270 fact, higher potential transport of sediments is expected if the volume of release
 271 generating the dense current increases.

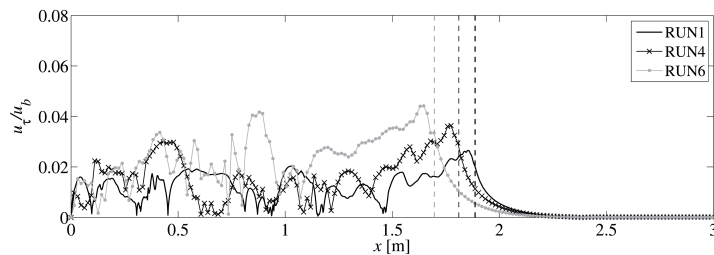


Figure 6: Dimensionless friction velocity for different runs ($\theta = 1.4^\circ$) after the gravity currents have travelled the same distance ($x_f - x_0 = 2$ m): effect of the variation of R . Vertical dashed lines mark the front position of the gravity currents.

272 3.3. The near-wall region

273 The turbulent structures of a lock-release gravity current developing in the
 274 near-wall region of the boundary layer are herein analysed. The dynamics occur-
 275 ring in the bottom region are important to understand how a gravity current
 276 is able to entrain bed particles along its path, as well as to analyse mixing
 277 processes. The fluctuating streamwise velocity $u'(x, y, z, t)$ is defined as

$$u' = u - \langle u \rangle \quad (13)$$

278 The distribution of u' on the plane closest to the bottom (at $y^* = y/H =$
 279 0.001) is shown in Figs. 7 and 8 for RUN0 ($R = 2$, $\theta = 0^\circ$) and RUN3 ($R = 2$,
 280 $\theta = 5^\circ$), respectively. In both figures the contours of u' are made dimensionless
 281 by u_b . At the beginning of RUN0 the intensity of the velocity fluctuations is
 282 high, particularly in the nose region of the gravity current (Fig. 7a), and it de-
 283 creases in time (Figs. 7b-d). Elongated turbulent structures form at the front
 284 of the dense current and develop in the head region (Fig. 7). The presence
 285 of these elongated turbulent structures may suggest that potential erosion de-
 286 velop along these longitudinal lines characterized by an excess of stress. These
 287 structures gradually decrease in intensity along the upstream direction and ul-
 288 timately vanish in the body region. Explosive blotches of turbulence are also
 289 visible in Fig. 7a at $x = 0.5$ m and in Fig. 7b at $x = 1$ m (i.e. $x^* = x/x_0 = 5$
 290 and $x^* = 10$, respectively). These areas are related to the presence of fully

291 developed Kelvin-Helmholtz billows. In fact, during the slumping phase, the re-
 292 gion characterized by elongated structures is sometimes broken by the presence
 293 of the Kelvin-Helmholtz structures. The three-dimensional density iso-surface
 294 corresponding to $\rho^* = 0.02$ is shown in Figs. 9a and 9b for RUN0 at $T^* = 17.1$
 295 and $T^* = 38.6$, respectively. In Fig. 9a Kelvin-Helmholtz billows occur at the
 296 interface between the two fluids, while in Fig. 9b the density iso-surface exhibits
 297 a more three-dimensional pattern. Lobe-and-cleft structures, due to the no-slip
 298 boundary condition at the bottom, are visible at the nose of the gravity current.
 299 Finally, in both Figs. 9a and 9b, the interaction between the billows formed at
 300 the interface and the turbulent structures developing in the near-wall region is
 301 visible. During the slumping phase, the mean length of the elongated turbulent
 302 structures is around 3 lock-lengths (Fig. 7a). Subsequently, they vanish in the
 303 body of the current and, due to the absence of Kelvin-Helmholtz billows in the
 304 head of the current, the mean length of these structures is about $4 x_0$ (Figs. 7
 305 b-d). In RUN3, elongated structures are less discernible and are shorter than
 306 in RUN0. During the slumping phase (Fig. 8a), elongated turbulent structures
 307 form at the nose of the gravity current and are qualitatively similar to those
 308 described in the horizontal case. After that, a fully developed but short re-
 309 gion with elongated structures of about 1.5 lock-lengths is clearly visible (Fig.
 310 8b), together with explosive blotches of turbulence structures occurring only in
 311 the body of the current. This region rapidly decreases in length at later times
 312 (Fig. 8c), until it disappears at the end of the simulation (Fig. 8d) when tur-
 313 bulent activity vanishes. The turbulent structures visible in Figs. 8c and 8d
 314 in the tail region of the gravity current are related to the backward flow oc-
 315 ccurring in the upsloping simulations. The three-dimensional density iso-surface
 316 is shown in Fig. 10 for RUN3 at the times $T^* = 18.6$ and $T^* = 31.3$. The
 317 presence of the Kelvin-Helmholtz instabilities is also visible for RUN3 in Fig.
 318 10a, and the billows appear smaller in size and more in number than in the
 319 horizontal case. After, the interface between the dense and the ambient fluids
 320 is characterized by fully developed turbulent structures and the flow becomes
 321 more three-dimensional, as visible in Fig. 10b. The near-wall region is rele-

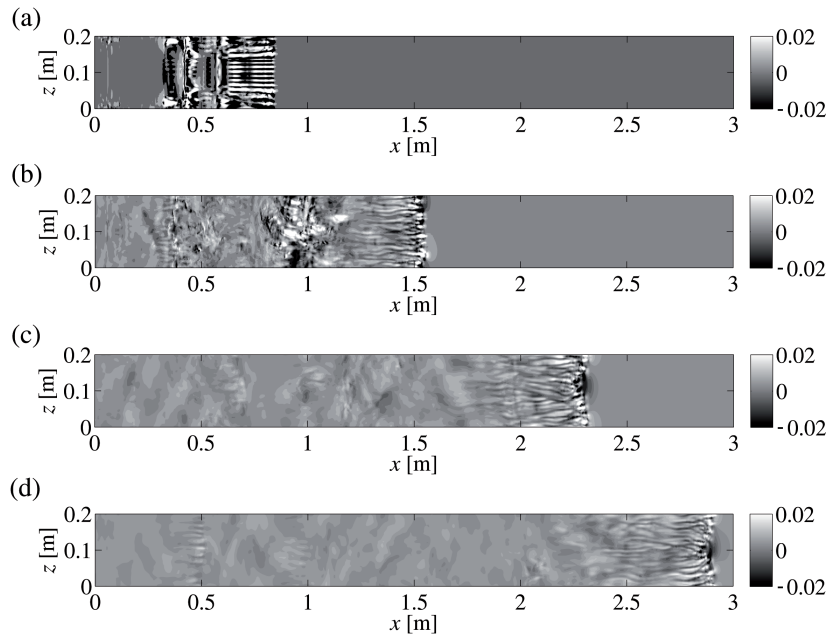


Figure 7: Dimensionless fluctuating velocity u'/u_b on the plane corresponding to $y^* = 0.001$ at different times for RUN0 ($R = 2$, $\theta = 0^\circ$): (a) $T^* = 17.1$; (b) $T^* = 38.6$; (c) $T^* = 65.9$; (d) $T^* = 90$.

322 vant for mixing and sediment transport when elongated turbulent structures
 323 and blotches structures are clearly discernible in the gravity current, i.e. during
 324 the slumping and during the beginning of the self-similar phases, in particular
 325 in the head and in the body regions. On the other hand, the near-wall region
 326 in the tail of the dense current is less effective in terms of mixing and sediments
 327 resuspension, particularly at later times of the simulations.

328 In the other cases (not shown) a similar behaviour is observed: pronounced and
 329 well-defined elongated structures characterized by an excess of stress are visible
 330 in the head region, suggesting that potential erosion is intensified along these
 331 lines, while the tail region is characterized by low and non-structured values of
 332 u' . In all the cases analysed, for fixed values of R , the length and the intensity of
 333 the elongated turbulent structures are affected by the inclination of the bottom,
 334 decreasing when θ increases.

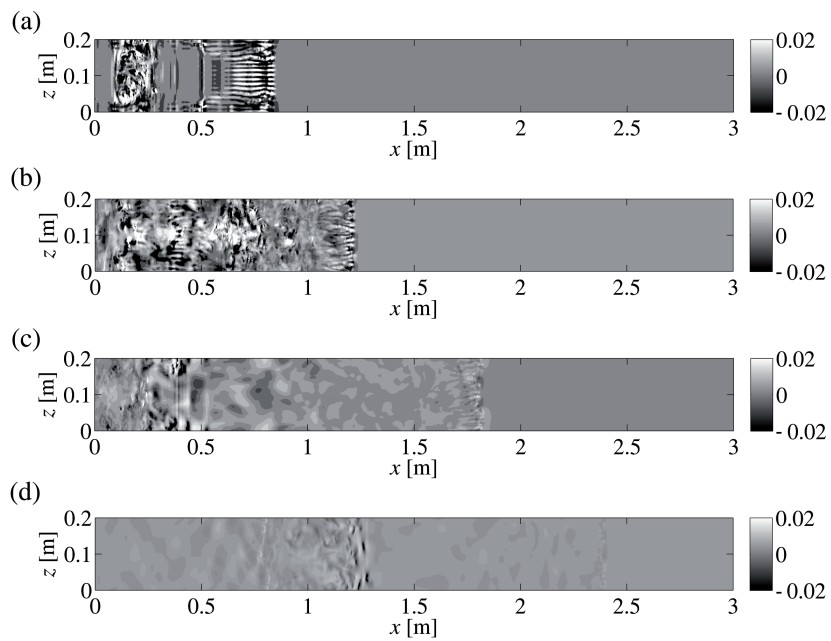


Figure 8: Dimensionless fluctuating velocity u'/u_b on the plane corresponding to $y^* = 0.001$ at different times for RUN3 ($R = 2$, $\theta = 5^\circ$): (a) $T^* = 18.6$; (b) $T^* = 31.3$; (c) $T^* = 65.4$; (d) $T^* = 145.7$.

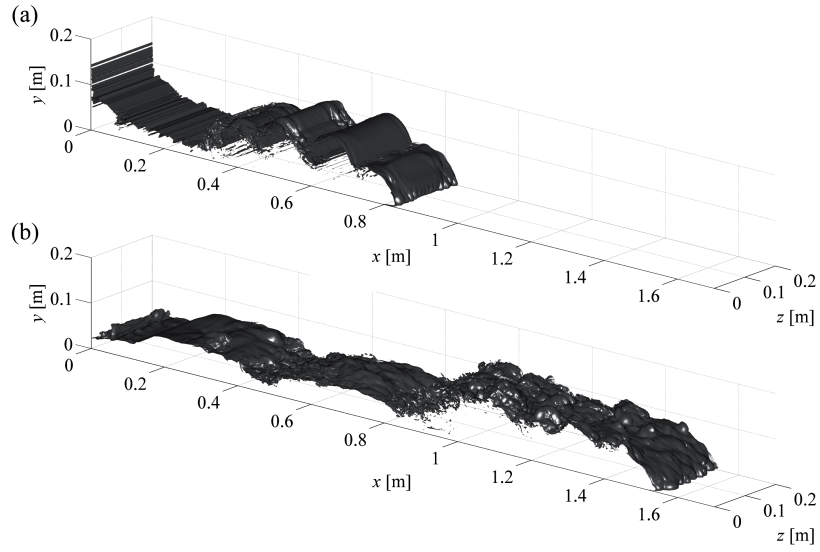


Figure 9: Three-dimensional density iso-surface, $\rho^* = 0.02$, for RUN0 ($R = 2$, $\theta = 0^\circ$): (a) $T^* = 17.1$; (b) $T^* = 38.6$.

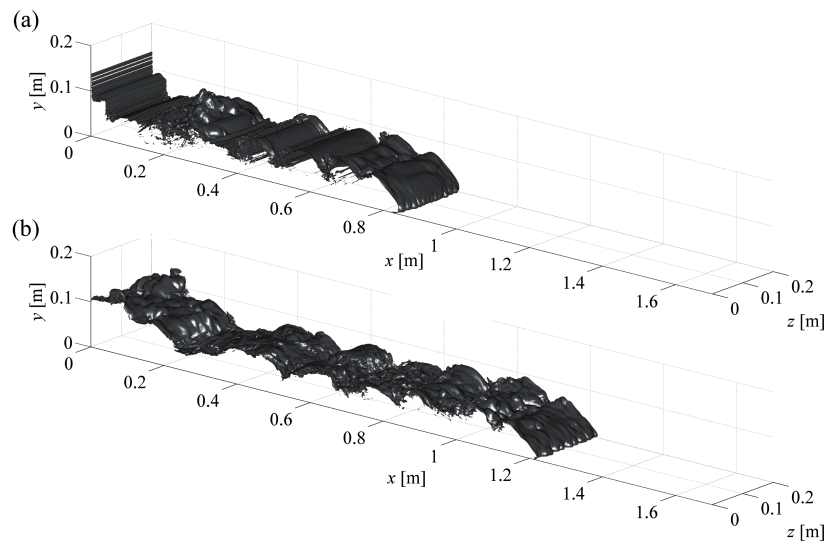


Figure 10: Three-dimensional density iso-surface, $\rho^* = 0.02$, for RUN3 ($R = 2$, $\theta = 5^\circ$): (a) $T^* = 18.6$; (b) $T^* = 31.3$.

335 *3.4. The turbulent kinetic energy*

336 In gravity currents, turbulence is generated by two different mechanisms
 337 occurring in two different regions, namely in the mixing layer at the interface
 338 between the heavy and light fluids and in the bottom region where a transitional
 339 boundary layer develops. Here we discuss production/dissipation terms of the
 340 turbulent kinetic energy budget in the above mentioned regions to highlight
 341 the role of the two different mechanisms in vertical mixing within the gravity
 342 current. The turbulent kinetic energy k is defined as:

$$k = \frac{1}{2} \langle u'_i u'_i \rangle \quad (14)$$

343 The transport equation for the resolved-scale turbulent kinetic energy is:

$$\frac{\partial k}{\partial t} + \langle u_j \rangle \frac{\partial k}{\partial x_j} = P + B - \epsilon + \frac{\partial T_j}{\partial x_j} \quad (15)$$

344 where T_j represent transport terms, the resolved buoyancy flux B is:

$$B = -\frac{g}{\rho_0} \langle \rho' v' \rangle \quad (16)$$

345 the production P extracting energy from the mean flow is defined as:

$$P = -\langle u'_i u'_j \rangle \frac{1}{2} \left(\frac{\partial \langle u_i \rangle}{\partial x_j} + \frac{\partial \langle u_j \rangle}{\partial x_i} \right) \quad (17)$$

346 and the dissipation rate ϵ is:

$$\epsilon = \nu \left\langle \frac{\partial u'_i}{\partial x_j} \frac{\partial u'_i}{\partial x_j} \right\rangle \quad (18)$$

347 This is a non-equilibrium unsteady turbulent flow, thus all terms of Eq. 15
 348 may contribute to development of the turbulent field. However here we look at
 349 the mechanism of production/destruction of turbulence, represented by the three
 350 terms P , B , ϵ . The source/sink contributions P , B and ϵ are shown in Fig. 11
 351 at $T^* = 17.1$ for the horizontally propagating gravity current (RUN0: $R = 2$,
 352 $\theta = 0^\circ$). In Fig. 11a the contour plot of k , made dimensionless with u_b^2 , is
 353 presented. The zones characterized by higher values of k are in correspondence

354 of the Kelvin-Helmholtz billows, in particular during their collapse. Very high
 355 values of k are visible also at the front of the dense current and in the area
 356 close to the interface between the current and the ambient fluid. Also the near-
 357 wall area shows relevant values of k , in particular under the nose of the gravity
 358 current, in agreement with the presence of the streaky structures discussed
 359 above.

360 The contour plots of B , P and ϵ , made dimensionless by u_b^3/H , are shown in
 361 Figs. 11b, 11c and 11d, respectively. B takes into account the effects of the
 362 buoyancy fluxes on k . Positive values of B indicate an unstable configuration
 363 in terms of buoyancy, leading to the production of turbulent kinetic energy.
 364 Negative values of B , on the other hand, are related to a stable configuration,
 365 acting toward suppression of k . Fig. 11b shows positive values of B at the
 366 nose of the gravity current, where an unstable configuration of density is found,
 367 and it is a source of k . Both positive and negative values of B are visible in
 368 correspondence of the Kelvin-Helmholtz instabilities. The rest of the body of
 369 the dense current is characterized by null and negative values of B , indicating a
 370 sink for k . P is the production of turbulent kinetic energy directly coming from
 371 the mean flow. In Fig. 11c, P has a spot-like behaviour, and positive production
 372 of k is visible near the Kelvin-Helmholtz billows and close to the bottom region.
 373 Relevant values of P are also observed in correspondence of the nose of the
 374 gravity current. ϵ is shown in Fig. 11d. The zones of the gravity current
 375 involved in the dissipation processes are in the head of the gravity current, at
 376 the bottom and at the interface with the ambient fluid. The evolution in time of
 377 ϵ exhibits that, for most of the duration of the simulations, while in the bottom
 378 region only a thin layer at the nose of the current is affected by dissipation,
 379 at the interface between the dense and the ambient fluids the dissipating layer
 380 is thicker (not shown). Finally, as expected, the strongest dissipation is found
 381 during the collapse of Kelvin-Helmholtz billows.

382 The evolution in time of the dimensionless k for RUN0 ($R = 2$, $\theta = 0^\circ$) and
 383 RUN2 (the case with $R = 2$ and $\theta = 2.5^\circ$, in which the front of the current
 384 reaches the end of the domain) are shown in Figs. 12 and 13, respectively.

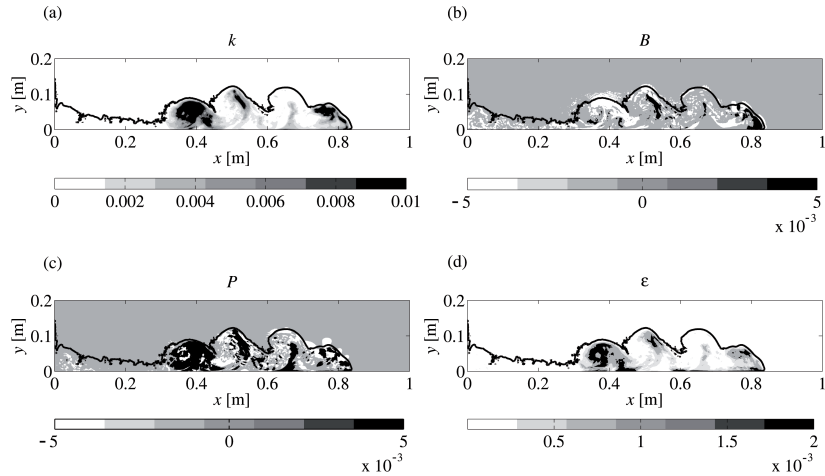


Figure 11: Spatial distribution of the terms contributing in the turbulent kinetic energy budget (RUN0: $R = 2$, $\theta = 0^\circ$. $T^* = 17.1$): (a) k ; (b) B ; (c) P ; (d) ϵ .

385 During the slumping phase of both runs, high values of k are visible in the head
386 region and in correspondence of the Kelvin-Helmholtz instabilities (Figs. 12a
387 and 13a). k decreases in time during the subsequent self-similar phase. The
388 distribution of k in the gravity current of both runs indicates that turbulence
389 is more effective in the region close to the ambient fluid, characterized by the
390 presence of the shear layer (Figs. 12b, 12c and 13b, 13c). At the beginning
391 of the self-similar phase, the presence of a collapsing Kelvin-Helmholtz billow
392 is evident at the distance of about 10 lock-lengths in both RUN0 and RUN2
393 ($x = 1$ m in Fig. 12b and $x = 1.2$ m in Fig. 13b). As expected, the decrease
394 of k is faster for gravity currents propagating up a slope than in the horizontal
395 case. In RUN2 the turbulent kinetic energy is about half the value of RUN0
396 (Figs. 12c and 13c), with $k > 0$ in the head region and k negligible in the rest
397 of the body of the current (Fig. 13c). At the end of RUN0 only the head of
398 the gravity current shows high values of k (Fig. 12d). At $T^* = 122.7$ of RUN2
399 (Fig. 13d) k is negligible in most of the dense current and low values of k are
400 found in a restricted area at the leading edge of the head of the current.

401 The contour plots of k , at different times, for RUN7 ($R = 0.67$, $\theta = 2.5^\circ$) are

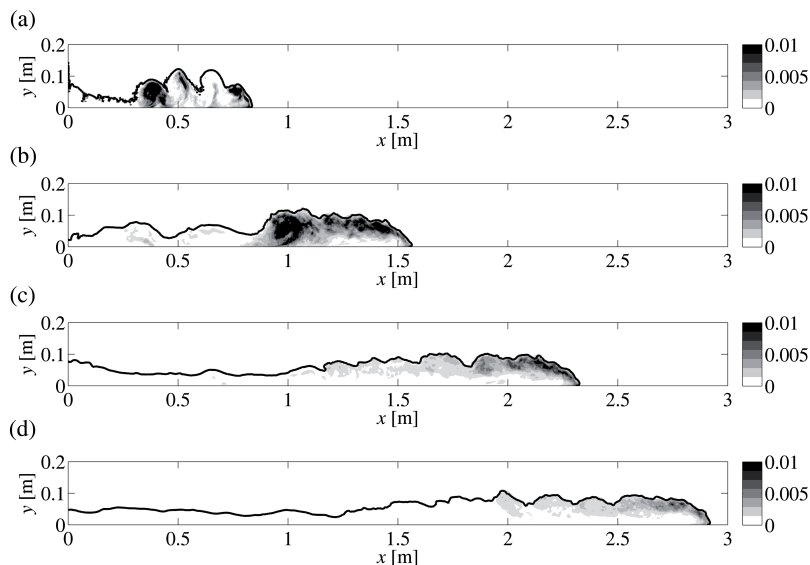


Figure 12: Turbulent kinetic energy at different times for RUN0 ($R = 2$, $\theta = 0^\circ$): (a) $T^* = 17.1$; (b) $T^* = 38.6$; (c) $T^* = 65.9$; (d) $T^* = 90$. Values of k are made dimensionless by u_b^2 .

402 shown in Fig. 14. High values of the turbulent kinetic energy are observed for
 403 RUN7, during all the propagation of the gravity current. It is worth mentioning
 404 that in RUN7, only the slumping phase and the early beginning of the self-
 405 similar phase occur. For this, high velocities are observed in RUN7 ($R = 0.67$,
 406 $\theta = 2.5^\circ$) in spite of the presence of an inclined surface, and the intensity
 407 of turbulence is higher than in the $R = 2$ case with the same θ (RUN2). A
 408 reduction of k is observed only at the end of the simulation (Fig. 14d), but high
 409 values are still visible in the head region close to the interface with the ambient
 410 fluid.

411 In all simulations, the turbulent contributions B , P and ϵ , characterizing the
 412 different regions of the gravity current as described above in Fig. 11 ($T^* = 17.1$),
 413 decrease in time, especially during the self similar phase (not shown). The
 414 decrease is more pronounced for higher values of θ . The evolution in time and
 415 the magnitude of the turbulent quantities are both affected by the variation

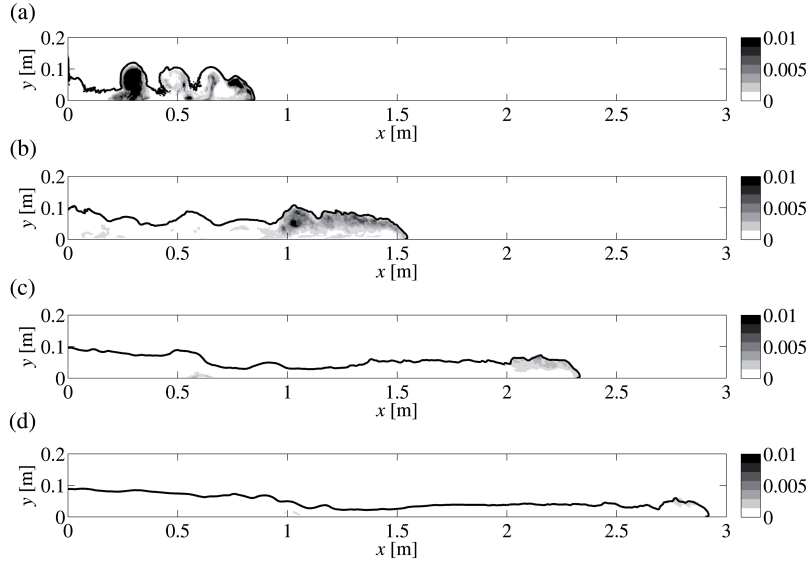


Figure 13: Turbulent kinetic energy at different times for RUN2 ($R = 2$, $\theta = 2.5^\circ$): (a) $T^* = 17.9$; (b) $T^* = 41.1$; (c) $T^* = 80.2$; (d) $T^* = 122.7$. Values of k are made dimensionless by u_b^2 .

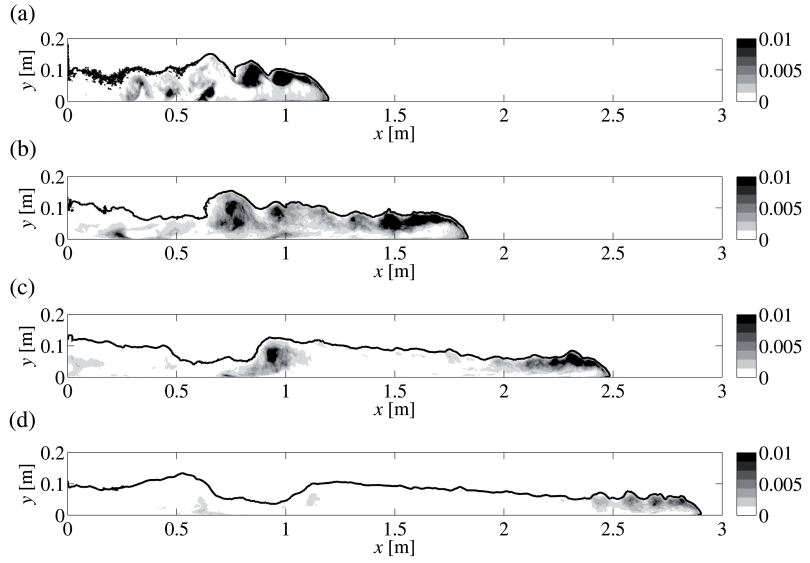


Figure 14: Turbulent kinetic energy at different times for RUN7 ($R = 0.67$, $\theta = 2.5^\circ$): (a) $T^* = 6.9$; (b) $T^* = 12.1$; (c) $T^* = 17.9$; (d) $T^* = 22.7$. Values of k are made dimensionless by u_b^2 .

416 of R : the smaller is the released volume, the faster is the decrease of the B ,
 417 P and ϵ . In particular, during the slumping phase B is positive at the nose
 418 of the gravity current and where the Kelvin-Helmholtz instabilities develop,
 419 while at later times B is negative in most of the body of the gravity current,
 420 indicating suppression of turbulent kinetic energy. The production of turbulent
 421 kinetic energy has an irregular distribution in all of the cases investigated. At
 422 the beginning of the simulations, Kelvin-Helmholtz billows lead to a production
 423 of turbulent kinetic energy, while during the self-similar phase production of
 424 k is found at the head of the gravity currents and $P \leq 0$ in the rest of the
 425 current. The sloping boundary inhibits high values of velocity and turbulence
 426 is reduced: the flow tends to stabilization and the production of turbulence is
 427 practically absent. Significant values of ϵ are visible during the slumping phase
 428 in correspondence of the Kelvin-Helmholtz billows, in the region close to the
 429 bottom of the domain and in the area close to the interface between the dense
 430 and the light fluids. At later times, ϵ decreases, and dissipation is observed only
 431 in the interface region. In the upsloping cases, the dissipative term decreases
 432 abruptly, until it almost vanishes at the end of the simulations.

433 4. Conclusions

434 The kinematics of lock-release gravity currents flowing up a slope were anal-
 435 ysed in terms of both mean flow and turbulent quantities, by varying the in-
 436 clination of the sloping bottom and the aspect ratio of the initial volume of
 437 release. The velocity fields were investigated revealing the presence of a back-
 438 ward flow in the near-wall region. The backward flow, qualitatively observed in
 439 literature, was here analysed in detail: the intensity of the negative values of $\langle u \rangle$
 440 increased as the inclination of the bottom increased, while the backward flow
 441 Q^- was only partially affected by θ because, although $\langle u \rangle$ increased in module
 442 with θ , $h(x, t)$ was inversely proportional to the slope. In fact, the gravity cur-
 443 rent became thinner and thinner with increasing θ and the interface between
 444 the dense and the ambient fluids became smoother, indicating the development

445 of a reduced turbulent pattern of the flow. The inspection of the dimensionless
446 friction velocity may suggest that the tail region of the gravity current plays a
447 fundamental role in the transport of sediments. In fact, values of the wall-shear
448 stress higher than those found in the head region were detected in the tail when
449 θ was high, revealing a relevant potential motion of sediments in the opposite
450 direction of the current's. Thus, the analysis of the mean velocity fields revealed
451 that the up-sloping bed thoroughly affects the dynamics of the current and that
452 the potential sediment transport intensity and direction depend on the slope
453 and R .

454 The inspection of the fluctuating streamwise velocity component allowed the vi-
455 sualization of elongated turbulent structures developing in the near-wall region.
456 Turbulent elongated structures were displayed, showing the importance of the
457 boundary layer in terms of transport of sediments in the head and in the body
458 regions, particularly during the first part of the simulations. The signature of
459 these elongated structures highlight a selective scour process, developing along
460 longitudinal erosive regions. The interaction between the Kelvin-Helmholtz bil-
461 lows developing at the interface and the turbulent structures in the near-wall
462 region was also shown, by the visualization of three-dimensional iso-density sur-
463 faces. The contour plots of k , B , P and ϵ were shown in order to detect the
464 different regions of the gravity current involved in the turbulent kinetic energy
465 balance. The areas of the current characterized by high values of k were at the
466 interface between the dense and the ambient fluids, particularly in the head re-
467 gion during the slumping phase and in correspondence of the Kelvin-Helmholtz
468 billows. The term of production associated to the buoyancy fluxes B was par-
469 ticularly important at the nose of the dense current, while it represented a sink
470 for k in the rest of the body of the gravity current. The production P related to
471 the velocity gradients of the mean flow was relevant close to the interface with
472 the ambient fluid, mainly in the head region and in the areas where Kelvin-
473 Helmholtz billows developed. Finally, the dissipation ϵ characterized the dense
474 current both in the near-wall region close to the nose of the gravity current
475 and in the head region, mainly at the interface with the ambient fluid. All

476 these terms decreased in time for the cases analysed. Moreover, their values
477 get smaller and smaller increasing the steepness of the bottom boundary and R ,
478 indicating that turbulence was affected by the presence of the sloping boundary.
479 Thus, also the turbulent structures are affected by the presence of an up-sloping
480 bed, decreasing in intensity with the increase of θ and R .

481

482 **Acknowledgments**

483 Funding: CA was supported by the PRACE Preparatory access 2015: [“Large
484 Eddy Simulation of unsteady gravity currents and implications for mixing.” Proposal
485 number 2010PA2821]; VA has been partially supported by the project “progetto
486 bandiera RITMARE.”

487 **References**

- 488 Adduce, C., Sciortino, G., & Proietti, S. (2012). Gravity currents produced by
489 lock exchanges: Experiments and simulations with a two-layer shallow-water
490 model with entrainment. *J. Hydraul. Eng.-ASCE*, *138*, 111–121.
- 491 Armenio, V., & Sarkar, S. (2002). An investigation of stably stratified turbulent
492 channel flow using large-eddy simulation. *J. Fluid Mech.*, *459*, 1–42.
- 493 Cantero, M., Balachandar, S., García, M., & Bock, D. (2008). Turbulent struc-
494 tures in planar gravity currents and their influence on the flow dynamics.
495 *Journal of Geophysical Research: Oceans (1978–2012)*, *113*.
- 496 Cantero, M., Lee, J., Balachandar, S., & Garcia, M. (2007). On the front
497 velocity of gravity currents. *J. Fluid Mech.*, *586*, 1–39.
- 498 Chang, Y. S., Xu, X., Özgökmen, T. M., Chassignet, E. P., Peters, H., & Fischer,
499 P. F. (2005). Comparison of gravity current mixing parameterizations and
500 calibration using a high-resolution 3d nonhydrostatic spectral element model.
501 *Ocean Modelling*, *10*, 342–368.

- 502 Dai, A. (2013). Experiments on gravity currents propagating on different bottom
503 slopes. *J. Fluid Mech.*, *731*, 117–141.
- 504 Dai, A. (2015). High-resolution simulations of downslope gravity currents in the
505 acceleration phase. *Phys. Fluids*, *27*, 076602.
- 506 Dai, A., & Huang, Y.-l. (2016). High-resolution simulations of non-boussinesq
507 downslope gravity currents in the acceleration phase. *Physics of Fluids (1994-
508 present)*, *28*, 026602.
- 509 Dai, A., Ozdemir, C., Cantero, M., & Balachandar, S. (2012). Gravity currents
510 from instantaneous sources down a slope. *J. Hydraul. Eng.*, *138*, 237–246.
- 511 Härtel, C., Meiburg, E., & Necker, F. (2000). Analysis and direct numerical
512 simulation of the flow at a gravity-current head. part 1. flow topology and
513 front speed for slip and no-slip boundaries. *J. Fluid Mech.*, *418*, 189–212.
- 514 Ilıcak, M. (2014). Energetics and mixing efficiency of lock-exchange flow. *Ocean
515 Modelling*, *83*, 1–10.
- 516 Inghilesi, R., Ottolenghi, L., Orasi, A., Pizzi, C., Bignami, F., & Santoleri, R.
517 (2012). Fate of river tiber discharge investigated through numerical simulation
518 and satellite monitoring. *Ocean Science Discussions*, *9*, 1599.
- 519 Jones, C. S., Cenedese, C., Chassignet, E. P., Linden, P. F., & Southerland,
520 B. R. (2015). Gravity current propagation up a valley. *J. Fluid Mech.*, *762*,
521 417–434.
- 522 Kneller, B., Bennett, S., & McCaffrey, W. (1999). Velocity structure, turbulence
523 and fluid stresses in experimental gravity currents. *J. Geophys. Research:
524 Oceans*, *104*, 5381–5391.
- 525 Kneller, B., & Buckee, C. (2000). The structure and fluid mechanics of turbidity
526 currents: a review of some recent studies and their geological implications.
527 *Sedimentology*, *47*, 62–94.

- 528 La Rocca, M., Prestininzi, P., Adduce, C., Sciortino, G., & Hinkelmann, R.
529 (2013). Lattice boltzmann simulation of 3d gravity currents around obstacles.
530 *International Journal of Offshore and Polar Engineering*, *23*, 178–185.
- 531 Legg, S., Hallberg, R. W., & Girton, J. B. (2006). Comparison of entrainment in
532 overflows simulated by z-coordinate, isopycnal and non-hydrostatic models.
533 *Ocean Modelling*, *11*, 69–97.
- 534 Lombardi, V., Adduce, C., Sciortino, G., & Rocca, M. L. (2015). Gravity cur-
535 rents flowing upslope: laboratory experiments and shallow water simulations.
536 *Phys. Fluids*, *27*, 016602.
- 537 Marleau, L. J., Flynn, M. R., & Sutherland, B. R. (2014). Gravity currents
538 propagating up a slope. *Phys. Fluids*, *26*, 046605.
- 539 Nogueira, H., Adduce, C., Alves, E., & Franca, M. (2013a). Analysis of lock-
540 exchange gravity currents over smooth and rough beds. *J. Hydraul. Res.*, *51*,
541 417–431.
- 542 Nogueira, H., Adduce, C., Alves, E., & Franca, M. (2013b). Image analysis
543 technique applied to lock-exchange gravity currents. *Meas. Sci. Technol.*, *24*,
544 047001.
- 545 Nogueira, H., Adduce, C., Alves, E., & Franca, M. (2014). Dynamics of the
546 head of gravity currents. *Environ. Fluid Mech.*, *14*, 519–540.
- 547 Ooi, S., Constantinescu, G., & Weber, L. (2009). Numerical simulations of
548 lock-exchange compositional gravity current. *J. Fluid Mech.*, *635*, 361–388.
- 549 Ottolenghi, L., Adduce, C., Inghilesi, R., Armenio, V., & Roman, F. (2016a).
550 Entrainment and mixing in unsteady gravity currents. *J. Hydraul. Res.*, *54*,
551 541–557.
- 552 Ottolenghi, L., Adduce, C., Inghilesi, R., Roman, F., & Armenio, V. (2016b).
553 Mixing in lock-release gravity currents propagating up a slope. *Phys. Fluids*,
554 *28*, 056604.

- 555 Özgökmen, T. M., Fischer, P. F., & Johns, W. E. (2006). Product water mass
556 formation by turbulent density currents from a high-order nonhydrostatic
557 spectral element model. *Ocean Modelling*, *12*, 237–267.
- 558 Özgökmen, T. M., Iliescu, T., & Fischer, P. F. (2009). Reynolds number depen-
559 dence of mixing in a lock-exchange system from direct numerical and large
560 eddy simulations. *Ocean Modelling*, *30*, 190–206.
- 561 Rottman, J., & Simpson, J. (1983). Gravity currents produced by instantaneous
562 releases of a heavy fluid in a rectangular channel. *J. Fluid Mech.*, *135*, 95–110.
- 563 Safrai, A. S., & Tkachenko, I. V. (2009). Numerical modeling of gravity currents
564 in inclined channels. *Fluid Dynamics*, *44*, 22–30.
- 565 Simpson, J. E. (1997). *Gravity currents: In the environment and the laboratory*.
566 Cambridge University Press.
- 567 Taylor, J. R., Sarkar, S., & Armenio, V. (2005). Large eddy simulation of stably
568 stratified open channel flow. *Phys. Fluids*, *17*, 116602.
- 569 Tokyay, T., Constantinescu, G., & Meiburg, E. (2011). Lock-exchange gravity
570 currents with a high volume of release propagating over a periodic array of
571 obstacles. *J. Fluid Mech.*, *672*, 570–605.